

Improved and Interpretable Solar Flare Predictions with Spatial & Topological Features of the Polarity-Inversion-Line Masked Magnetograms

Hu Sun¹, Ward Manchester IV², Yang Chen¹

¹Department of Statistics, University of Michigan, Ann Arbor

²Department of Climate and Space Sciences and Engineering, University of Michigan, Ann Arbor

Key Points:

- We adopt a polarity inversion line (PIL) detecting algorithm to obtain PIL masks for the B_r component and several SHARP parameter maps.
- We construct two sets of spatial statistics features and a collection of topological features based on the PIL masks.
- Our newly constructed features, by itself or joint with topological features, can significantly improve flare predictions than using SHARP parameters only.

Plain Language Summary:

Our research is targeted at improving the accuracy of solar flare classification by training machine learning models with new interpretable features beyond well-known physics-based predictors. We count the number of closed loops and calculate multiple summary statistics of the spatial distribution of high-resolution magnetic field images of solar active regions to boost the classification result of strong and weak flares. Our results reveal that the spatial distribution of local physical quantities derived from the magnetograms, beyond those commonly adopted, aggregated quantities, can be helpful to improve flare predictability.

Corresponding author: Yang Chen, ychenang@umich.edu

This is the author manuscript accepted for publication and has undergone full peer review but has not been through the copyediting, typesetting, pagination and proofreading process, which may lead to differences between this version and the [Version of Record](#). Please cite this article as [doi: 10.1029/2021SW002837](https://doi.org/10.1029/2021SW002837).

This article is protected by copyright. All rights reserved.

Abstract

Many current research efforts undertake the solar flare classification task using the Space-weather HMI Active Region Patch (SHARP) parameters as the predictors. The SHARP parameters are scalar quantities based on spatial average or integration of physical quantities derived from the vector magnetic field, which loses information of the two-dimensional spatial distribution of the field and related quantities. In this paper, we construct two new sets of spatial features to expand the feature set used for the flare classification task. The first set uses the idea of topological data analysis to summarize the geometric information of the distributions of various SHARP quantities across active regions. The second set utilizes tools coming from spatial statistics to analyze the vertical magnetic field component B_r and summarize its spatial variations and clustering patterns. All features are constructed within regions near the polarity inversion lines (PILs) and classification performances using the new features are compared against those using SHARP parameters (also along the PIL). We found that using the new features can improve the skill scores of the flare classification model and new features tend to have higher feature importance, especially the spatial statistics features. This potentially suggests that even using a single magnetic field component, B_r , instead of all SHARP parameters, one can still derive strongly predictive features for flare classification.

1 Introduction

Solar flares occur in regions of strong magnetic fields possessing concentrated free energy, which are susceptible to spontaneous reconnection that rapidly heats the plasma producing flare emission. At the photosphere these fields typically take the form of active regions that are characterized by strong horizontal field gradients, long and well defined polarity-inversion lines (PILs), and complex flux distributions (Falconer et al., 2002, 2003, 2006; Barnes et al., 2007; Schrijver, 2007, e.g.). Vector magnetogram observations reveal that the magnetic field runs nearly parallel to the PIL, where the field is in a configuration that possesses significant free energy to drive flares. In addition to the free energy content, the other critical feature related to flare onset is the magnetic field complexity represented by the intermixing of opposing magnetic flux. At the simplest level, such complexity is found in strong gradients along the PIL (Falconer et al., 2003; Schrijver, 2007) to more extreme cases of flare production in delta-spot active regions, which contain both polarities within single penumbra of uniform polarity. A well known example is active region numbered 10486, which produced a series of X-class flares in the fall of 2003.

The question naturally arises as to whether there are unique features which may serve as strong discriminators or predictors of flares. (Schrijver, 2007) found that the amount of unsigned flux within a distance of 15 Mm of the PIL was such a discriminator. Similar phenomenological studies have revealed a number of physical discriminators for flare production based solely on the observed line-of-sight component of the field (e.g. (Falconer, 2001; Falconer et al., 2002, 2006; Leka & Barnes, 2003a, 2003b; Barnes et al., 2007). These works describe scalar quantities that are measures of the unsigned magnetic flux and the length of the PIL, which have proven useful for flare prediction. In the case of Falconer (2002), four measures of magnetic free energy were derived based on 3-component vector magnetograms: the length of the PIL exhibiting strong shear, vertical electric current, total unsigned flux, and the current helicity. These works were followed by more elaborate flare prediction studies employing more than 20 scalar quantities derived from Space Weather HMI Active Region Patches (SHARPs), where HMI is the Helioseismic and Magnetic Imager for the Solar Dynamics Observatory (SDO), which we refer to as HMI/SDO hereafter. These SHARP variables are derived from largely-uninterrupted high-resolution high-cadence full disk vector magnetograms, which provide sufficient data for successful application of machine learning for flare prediction (e.g. Bobra et al. (2014); Bobra and Couvidat (2015); Nishizuka, Sugiura, Kubo, Den, and Ishii (2018); Liu, Deng,

75 Wang, and Wang (2017); Florios et al. (2018); Y. Chen et al. (2019); J. Wang et al. (2020);
76 Jiao et al. (2020)).

77 Statistical analysis typically strives to determine discriminant functions which may
78 be linear or nonlinear functions of variables constructed from the observed vector mag-
79 netic field, which are related to distributions of free energy in the system. Flares follow
80 from two processes: firstly the buildup of free magnetic energy and secondly the release
81 of that energy by magnetic reconnection. For the first component there are meaningful
82 measures of buildup of energy necessary for flare occurrences such as the active region
83 (AR) size as denoted by unsigned magnetic flux and total electric current, current heli-
84 city or total free energy itself. Numerous studies illustrates (e.g. (Leka & Barnes, 2003b;
85 Barnes et al., 2016; Leka et al., 2019b, 2019a; Y. Chen et al., 2019) . However, whether
86 it is sufficient to produce a flare involves much more subtlety as it relates to the com-
87 plexity of the magnetic field which ties into the formation of current sheets, which ini-
88 tiates the flare energy release. Because of this complexity of the reconnection process,
89 there can be a wide range of free energy densities found in flaring ARs, which empha-
90 sizes the challenging aspect of predicting flares.

91 In recent years, data-driven flare forecasting has caught much attention in the field
92 of space sciences. Many machine learning algorithms have been adopted for solar flare
93 prediction, either with or without operational forecasting in mind (Barnes et al., 2007).
94 Bobra et al. (2014) introduced the Space-weather HMI Active Region Patch (SHARP)
95 parameters, which are derived from HMI/SDO vector magnetograms and have been used
96 by many solar flare prediction models in recent years (e.g. (Bobra & Couvidat, 2015; Barnes
97 et al., 2016; Muranushi et al., 2016; Florios et al., 2018; Nishizuka et al., 2018; Leka &
98 Barnes, 2018; Y. Chen et al., 2019; Liu et al., 2019; Leka et al., 2019b, 2019a; Campo-
99 reale, 2019; Jiao et al., 2020; Nishizuka et al., 2021). The success of using the SHARP
100 parameters in solar flare forecasting showcases the importance of these parameters to
101 the triggered solar eruptions. Despite this success, the SHARP parameters may not cap-
102 ture the full information of the HMI/SDO magnetogram images, which is relevant for
103 flare forecasting. To directly analyze the magnetograms, there are efforts using deep neu-
104 ral network methods, which directly employ HMI/SDO magnetogram images to predict
105 solar eruptions (e.g. the Long Short Term Memory network adopted by Y. Chen et al.
106 (2019) and Liu et al. (2019)). The neural network models, however, suffer from poor in-
107 terpretability, making it difficult to learn new insights of the underlying physics/mechanism
108 of flare eruptions from those models. In an effort to obtain an interpretable solar flare
109 forecasting model, while at the same time pushing the frontiers of discovering new physics
110 of solar eruptions, we present our new results and findings on constructing spatial and
111 topological features that are important for solar flare predictions, from the magnetograms
112 of HMI/SDO.

113 In Y. Chen et al. (2019), it was shown that features derived from a deep neural net-
114 work (autoencoder) can give similar performance to the SHARP parameters when adopted
115 to solar flare predictions. However, one cannot conclude that the SHARP parameters
116 contain all useful magnetogram information. Flare predictions for general-purpose im-
117 age/video feature reduction techniques typically result in high-dimensional, highly cor-
118 related features, many of which are redundant for flare predictions. To alleviate this is-
119 sue, efficient dimension reduction and feature selection techniques are adopted in Y. Chen
120 et al. (2019). However, the amount of random noise brought in with this high-dimensional
121 feature construction with limited amount of training data still makes the performance
122 not ideal. Meanwhile, it is important to realize that even in this unfavorable situation
123 of directly extracting features from magnetograms, we can achieve similar flare predic-
124 tion performance when using only the SHARP parameters. This possibility makes it prom-
125 ising to further investigate alternative feature construction methods that result in infor-
126 mation complementary to those already contained in the SHARP parameters.

127 More recently, some promising results have already been shown along this direc-
 128 tion: in Deshmukh, Berger, Meiss, and Bradley (2020), topological features are derived
 129 for the B_r component, which are shown to improve the performance of flaring active re-
 130 gion predictions on top of SHARP parameters. More precisely, they count the number
 131 of “loops” formed by high- B_r pixels from the B_r component as a flare predictor, a.k.a.
 132 the topological features referred therein.

133 Here, we extend this approach by combining both spatial and topological features
 134 of the polarity inversion line masked magnetograms (HMI/SDO active regions) with the
 135 SHARP parameters for solar flare predictions. We show that the results of the predic-
 136 tion models are better when we use all three sets of features, and that the spatial statis-
 137 tics features are of key importance. Furthermore, we point out the interpretations of the
 138 spatial statistics features and relate it back to the underlying mechanism of flare forma-
 139 tion, thus using these features to inform the discovery of new physics.

140 The remainder of this paper is organized as follows. In Section 2, we first give a
 141 motivating example to show the potential of extracting shape information from HMI im-
 142 ages for flare classification, then we describe the methodology and details of construct-
 143 ing topological features and spatial statistics features out of HMI images and the dis-
 144 tribution of SHARP quantities within active regions. In Section 3, we present the data
 145 used for empirical study and the prediction results based on newly constructed features
 146 and corresponding interpretations. Section 4 concludes.

147 2 Feature Construction

148 The SHARP parameters, as introduced in Bobra et al. (2014), contain several es-
 149 sential physical quantities calculated from the three-component, two-dimensional HMI
 150 magnetic field data of active regions. It is important to note that all the SHARP param-
 151 eters are scalar values summarizing physical quantities of the *whole* active region, which
 152 are calculated based on spatial averages (e.g. the MEANGAM) or spatial integration (e.g.
 153 the TOTUSJH). As a result, the SHARP parameters do not contain any information re-
 154 garding the spatial distribution of the physical quantities.

155 A refined version of the SHARP parameters taking into account some information
 156 of the spatial distribution is the SHARP parameters weighted by the polarity inversion
 157 line (PIL) mask, as given by J. Wang et al. (2020). We refer to these features as the PIL-
 158 weighted SHARP parameters in the following text. The PIL mask is a weighted mask
 159 which puts high weight on the region where the vertical component of the magnetic field
 160 is zero ($B_r = 0$), between regions of strong opposite polarity. Empirically, it is not prac-
 161 tical to accurately pinpoint all pixels with $B_r = 0$, so adjacent regions are also given
 162 smaller weights and overall the PIL mask is giving high weights to regions around the
 163 PIL and near-zero weight to other regions.

164 However localized, the PIL-weighted SHARP parameters still cannot reflect the spa-
 165 tial characteristics of the magnetic field, but merely be selective to information based
 166 on position. In this section, we introduce two sets of features constructed with the aim
 167 of augmenting the SHARP parameters by considering local spatial distribution of the
 168 magnetic field components around the polarity inversion line: one based on persistence
 169 homology in topology and the other is based on concepts from the field of spatial statis-
 170 tics. We will apply these newly constructed features to flare classification and develop
 171 their utility in context with existing literature on related topics, e.g. the weighted SHARP
 172 parameters by J. Wang et al. (2020) and the topological data analysis enabled feature
 173 construction by Deshmukh, Berger, Bradley, and Meiss (2020).

2.1 Motivating Example & PIL Mask Construction

To motivate our feature construction machinery, we start with a concrete example: comparing a strong and a weak flare that occurred in HARP region 377. In Figure 1, we show two rows of images with HMI magnetograms of HARP region 377, and two derived quantities. The top row is for an M class flare and the bottom for a B class flare. All images are collected 1 hour prior to the moment of peak flare intensity. Focusing on (a) and (d) first, one can see that before the M flare, the high magnetic flux pixels of opposing polarities are more clustered and concentrated in close proximity to one another. This distribution coincides with the formation of a well-defined polarity inversion line (PIL) (where $B_r = 0$) that separates the regions of opposing polarity. The PIL is picked up by the corresponding polarity inversion line mask shown in (b) and (e). PILs are the epicenter of flare activity and have been used as a discriminator of flare regions in prior studies (Falconer et al., 2006; J. Wang et al., 2019). We also focus on the PIL regions when distinguishing strong and weak flares.

We derive the PIL mask based on the method given in Schrijver (2007), which follows three steps. First, we produce two bitmaps, one for the positive field where pixels with $B_r > 200\text{G}$ are set to 1 and 0 otherwise, one for the negative field where pixels with $B_r < -200\text{G}$ are set to -1 and 0 otherwise. Second, we derive the positive and negative masks using a density-based clustering algorithm (Ester et al., 1996). Finally, we multiply the two masks after convolving each mask with a Gaussian kernel with a bandwidth of 10 pixels. Details of the derivations can also be found in J. Wang et al. (2019).

If one only compares the SHARP parameters, such as the total unsigned flux, the difference between the M flare and B flare is not necessarily significant because both flares have regions with relatively high B_r values. But if one focuses on the spatial distributions of regions of high B_r values, such as how clustered these regions are and what geometric shapes they form jointly and individually, then extra discriminating power for telling the flares apart would emerge. In the following two sub-sections, we will focus on the HMI magnetograms (the B_r component in particular) restricted to the PIL region (non-zero PIL weight region), for which we derive topological and spatial features. We concentrate on the PIL region since it removes many irrelevant regions outside of the flaring region (J. Wang et al., 2020) that can potentially create noises for the derived features.

Besides the B_r component, we also derive eight additional 2D SHARP quantity maps as follows. We still calculate the SHARP intensive physical quantities for every pixel, but instead of taking the averages or spatially integrating them to form the scalar SHARP parameters, we retain the 2D distribution of each of these maps and multiply it by the same B_r PIL mask. And we refer to these maps as **SHARP parameter maps** hereafter. Table 1 gives a summary of all nine SHARP parameter maps we collect/construct. We only include these nine SHARP parameter maps because they: 1) can be localized to every pixel; 2) can be thresholded with easy interpretations; 3) cover most of the “important features” based on many machine learning studies.

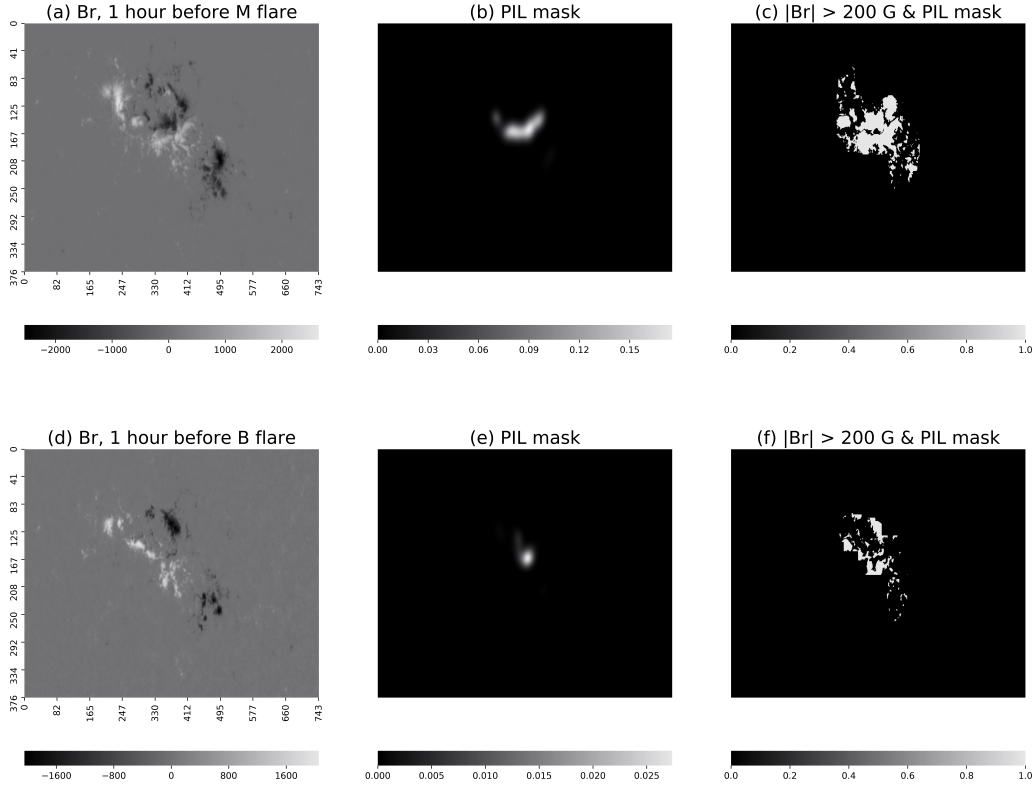


Figure 1. Two HMI magnetograms and derived images of HARP 377. The two rows consist of 3 related images: (left) the B_r component, (middle) the PIL weight mask, and (right) bitmap labeling pixels with absolute values of B_r over 200 G, which locate the PIL region. The top row is collected 1 hour before the M-class flare peaked at 2011.02.13 17:38:00 while the bottom row is collected 1 hour before the B-class flare peaked at 2011.02.13 00:42:00. Note the more energetic flare occurs at a later time when more flux has emerged and the PIL is significantly longer. Different scales are used to bring out structure in B_r and the PIL mask. Panel (c) and (f) appear to have a larger mask region when compared to the PIL mask shown in panel (b) and (e), which is due to the fact that many pixels that are also part of the PIL mask but have near-zero PIL weights, leading to their invisibility in the PIL masks.

Channel	Formula	Unit
Br	\mathbf{B}_z	G
GAM	$\arctan\left(\frac{\mathbf{B}_h}{\mathbf{B}_z}\right)$	Degree
GBT	$\sqrt{\left(\frac{\partial\mathbf{B}}{\partial x}\right)^2 + \left(\frac{\partial\mathbf{B}}{\partial y}\right)^2}$	$\text{G} \times \text{Mm}^{-1}$
GBH	$\sqrt{\left(\frac{\partial\mathbf{B}_h}{\partial x}\right)^2 + \left(\frac{\partial\mathbf{B}_h}{\partial y}\right)^2}$	$\text{G} \times \text{Mm}^{-1}$
GBZ	$\sqrt{\left(\frac{\partial\mathbf{B}_z}{\partial x}\right)^2 + \left(\frac{\partial\mathbf{B}_z}{\partial y}\right)^2}$	$\text{G} \times \text{Mm}^{-1}$
USJZ	$\left \left(\frac{\partial\mathbf{B}_y}{\partial x} - \frac{\partial\mathbf{B}_x}{\partial y}\right)\right $	A
USJH	$ \mathbf{J}_z \times \mathbf{B}_z $	$\text{G}^2 \text{ m}^{-1}$
POT	$\left((\mathbf{B}_x - \mathbf{B}_x^{POT})^2 + (\mathbf{B}_y - \mathbf{B}_y^{POT})^2\right)$	erg cm^{-3}
SHR	$\arccos\left(\frac{\mathbf{B}_x^{POT} \times \mathbf{B}_x + \mathbf{B}_y^{POT} \times \mathbf{B}_y + \mathbf{B}_z^2}{\sqrt{\mathbf{B}_x^{POT^2} + \mathbf{B}_y^{POT^2} + \mathbf{B}_z^2} \sqrt{\mathbf{B}_x^2 + \mathbf{B}_y^2 + \mathbf{B}_z^2}}\right)$	Degree

Table 1. SHARP parameter maps, where the formulas in the middle column are applied to every pixel of the HMI magnetogram. Here, $\mathbf{B}_x, \mathbf{B}_y, \mathbf{B}_z$ are the x, y, z components of the magnetic field and $\mathbf{B}_x^{POT}, \mathbf{B}_y^{POT}$ the potential field components respectively. Detailed definition of the SHARP parameters can be found in Table 3 of Bobra et al. (2014).

215 The same feature construction procedure is then applied to all nine SHARP pa-
 216 rameter maps, which are created by multiplying by the 2-D SHARP distributions by the
 217 PIL mask. For the topological features alone, our work using all nine SHARP param-
 218 eter maps can be seen as an extension to the topological data analysis in Deshmukh, Berger,
 219 Bradley, and Meiss (2020), which mainly focused on the original B_r component when
 220 constructing topological features. For spatial statistics features, which have not yet been
 221 adopted by others in literature as far as we are aware of, we only focus on the B_r com-
 222 ponent for the ease of interpretation. All of the features, both topological and spatial
 223 statistics features, are derived only for the PIL region. As a comparison, we use the PIL-
 224 weighted SHARP parameters as a benchmark feature set, which has been shown to im-
 225 prove flare predictions as compared to unweighted SHARP parameters (J. Wang et al.,
 226 2020).

227 We formulate the machine learning task in this study as strong (M/X) versus weak
 228 (B) flare binary classification. We exclude C-class flare samples to create a strong con-
 229 trast between the positive and negative classes, thus making the post-hoc interpretation
 230 more meaningful. We also exclude the non-flaring samples as it is hard to decide the amount
 231 of such “quiet time” samples in the training and testing set. An excessive amount of non-
 232 flaring samples would boost the final classification metrics. Also, including these sam-
 233 ples would make the model interpretation harder because the signals picked up by the
 234 features can be a hybrid of discriminators against quiet times and against weak flares.
 235 We limit our sample sets to M/X and B flares only to make the interpretation straight-
 236 forward. In the appendix, we give results when C-class flares are also included as an ex-
 237 tension.

2.2 Topological Features

The derivation of our topological features is based on the topological data analysis (TDA) in Deshmukh, Berger, Bradley, and Meiss (2020) and Deshmukh, Berger, Meiss, and Bradley (2020). They take the B_r component from both flaring ARs and non-flaring ARs, apply a series of B_r threshold values to every pixel and count the number of “loops” formed by the high-flux pixels above the thresholds. Loops are defined under the notion of cubical complex, which will be developed shortly. The number of loops under each threshold is used as a flaring region predictor.

Compared to the previous works, we have these extensions:

- we expand the image set to be analyzed from just the B_r mask to multiple other SHARP parameters maps,
- we restrict our TDA application to the PIL region only to remove noises in feature construction,
- we adopt the topological features for strong (M/X) versus weak (B) flare classification purpose.

In this subsection, we briefly review the methodology first and then highlight the differences of our data pipeline compared to existing literature.

Topological data analysis, a.k.a. TDA, (see Wasserman (2018) for a brief review) is a field investigating the mathematical shape of a point cloud or a function. It establishes the concept of topological invariance between objects that share the same topological property, such as a ball and cube, or a cup and a doughnut. TDA can be applied to analyze the 2D SHARP parameter maps since all SHARP parameters can be viewed as a 2D function with each pixel’s x and y coordinate being the functional input.

It is not practical to summarize all shape information of a function or a point cloud, and a very simple summary statistics in TDA about the topology property is the Betti number (Munch, 2017). Betti numbers, typically denoted as $\beta_0, \beta_1, \beta_2, \dots$, counts the number of holes of 0, 1, 2, \dots dimension. In 2D, β_0, β_1 represents the number of connected components and loops. These loops are closed curves formed at similar levels of B_r attained in the magnetogram rather than the more familiar coronal loops observed in the extreme ultraviolet. In our analysis, we just focus on the β_1 Betti number, counting the number of loops within the 2D SHARP parameter maps.

Because every 2D SHARP parameter map is a digitized image, it is not a continuous but a discretized surface. Therefore, we need a proper definition of loop in these 2D images. Take the B_r component as an example, if one thresholds the B_r image at various levels and only keeps pixels below the threshold and within the PIL region, forcing all other pixels as 0, one obtains distributions as found in Figure 2 shown below.

One can notice that around the center of each image, there are several closed loops coming into existence when one increases the threshold from 194.99G to 583.35G; and that some of the loops disappear while others remain but shrink in size when the threshold level is further increased to 918.35G. All these thresholds are the 30-th, 75-th and 90-th percentile of the pixel-level B_r across all data. We will elaborate on how to choose these thresholds empirically shortly. Intuitively, these loops are regions of high $|B_r|$ values within the PIL region, or in other words, they surround the peaks/valleys of the spatial distribution of B_r . This sequence of thresholded images forms a *filtration*, where the set of all nonzero pixels of one image is a subset of the nonzero pixels of the next image with a higher threshold.

To give these kinds of loops in a digitized image a rigorous definition, we invoke the concept of *cubical complex*, as suggested by Deshmukh, Berger, Bradley, and Meiss (2020). For every image with threshold τ as shown in Figure 2, we generate a correspond-

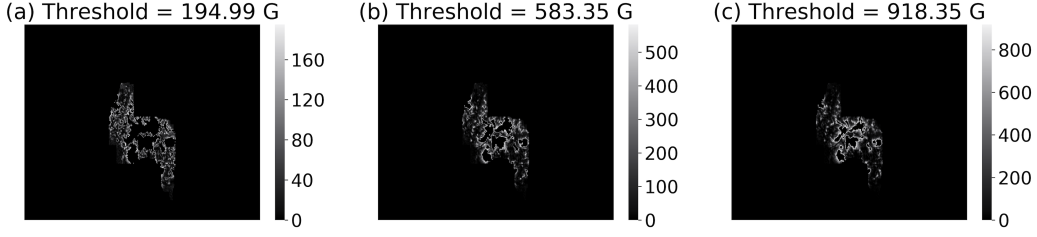


Figure 2. B_r component of HARP 377, 2011.02.13 17:38:00. (a), (b), (c) only keep pixels whose $|B_r|$ value is below the threshold (194.99G, 583.35G, 918.35G) and within the PIL region. The three thresholds are the 30-th, 75-th and 90-th percentile of the B_r values, at pixel level, across all data.

ing bitmap. Each bitmap sets all pixels that are: 1) below the threshold τ , 2) within the PIL region, as 1, and 0 otherwise. The loops are then defined for these bitmaps.

As a schematic example, in Figure 3 we show two bitmaps with red pixels being 1 and white pixels being 0. Sub-figures (a) and (b) show two bitmaps generated from a low and a high threshold value, respectively. In a cubical complex, two pixels are connected if they share an edge or vertex and a loop is a closed, hollow area surrounded by a series of connected pixels. In (a) we have two loops, labeled as 1 and 3. As we increase the threshold, those pixels above the low threshold but under the high threshold become red and some new loops are formed (loop 2 in (b)), some remain but shrink in size (loop 1 in both (a) and (b)) and some disappear (loop 3 in (a)).

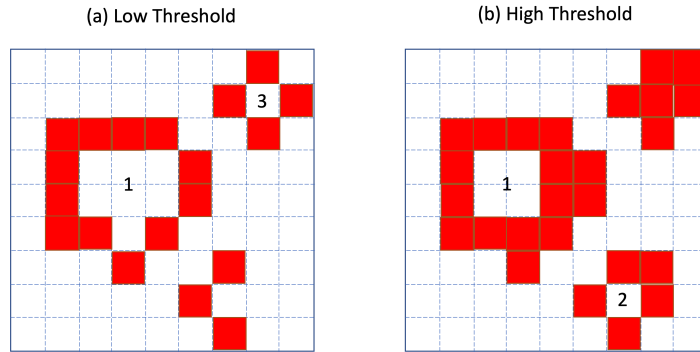


Figure 3. Example of loops formed by cubical complexes. In a cubical complex, two pixels are connected if they share a vertex or an edge. Panel (a) at a low threshold, there are two loops formed, labeled as 1 and 3. Panel (b) at a higher threshold, more pixels are selected (marked red), and loop 3 is closed, loop 2 comes into existence and loop 1 remains alive.

Every loop in this cubical complex has its own life-cycle. Each has a birth time and a death time, represented by the threshold values at which the loop emerges and disappears. A graph showing the birth-death pair of all loops is called the *persistence diagram* (Kaczynski et al., 2004; Ghrist, 2008; Zomorodian et al., 2012; Munch, 2017). When a loop has its death time much larger than the birth time, this loop indicates a strong peak/valley in the 2D distribution of a SHARP parameter map. Such loops appear as scattered points away from the 45 degree line in the persistence diagram. In Figure 4, we show the persistence diagrams for all loops of the B_r component of 3 flares coming from HARP re-

305 gion 377. One can see that compared to the two M flares, the persistence diagram of the
 306 B flare has loops that are way off the 45 degree line, indicating that there are fewer in-
 307 tense B_r regions prior to the B flare.

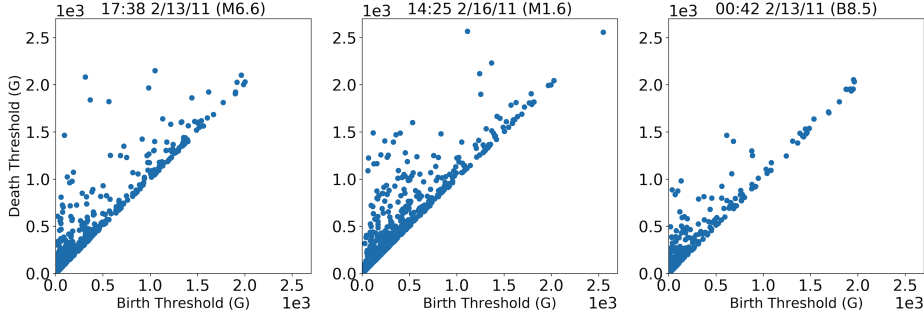


Figure 4. Examples of persistence diagrams for two M flares and a B flare of HARP region 377. Every subplot has the flare peak time, flare class and flare intensity in the title. One can see that compared to the M flares, the B flare has less loops that are persistent, indicating that there are fewer regions of intense B_r in the PIL region. All B_r masks analyzed are collected 1 hour prior to the flare time. Both axes in each plot have the unit Gauss.

308 In order to extract features, namely the Betti number β_1 , from such diagrams, we
 309 do the following. For every SHARP parameter map in Table 1, we first calculate the pixel-
 310 level percentiles at 5%, 10%, ..., 90%, 95% across all pixels of our dataset. For the B_r ,
 311 we do not distinguish between the positive and negative pixels but take the absolute value
 312 before calculating the Betti numbers. The percentiles for $|B_r|$ are: 19.4G, 42.8G, ..., 918.3G, 1165.8G.
 313 Other SHARP parameters have their corresponding percentiles. Then we derive the per-
 314 sistence diagram for every SHARP parameter map using the procedure above. Finally,
 315 we count, at each percentile, how many loops are still alive (Maria et al., 2014). Because
 316 we have 19 percentiles, we have 19 Betti number features, and since we have 9 SHARP
 317 maps, in total we obtain $19 \times 9 = 171$ topological features for a single flare.

318 2.3 Spatial Statistics Features

319 In the previous subsection, we reviewed the TDA analysis on SHARP parameter
 320 maps, which is able to summarise the shape information of the spatial distribution of
 321 the corresponding SHARP parameter maps. Using the Betti number β_1 as a summary
 322 statistics, we can locate the peaks/valleys of a spatial distribution of any SHARP pa-
 323 rameter. However, there are other aspects of the spatial distribution, such as the den-
 324 sity of high B_r pixels and the spatial variation of a SHARP quantity, that cannot be sum-
 325 marised by the TDA. *Spatial statistics* techniques (see Gelfand, Diggle, Guttorp, and Fuentes
 326 (2010) and references therein), on the other hand, provides natural tools to extract this
 327 information from spatial distributions. In our spatial statistics analysis, we focus on the
 328 B_r maps only for the sake of interpretability. The two relevant spatial statistics tools
 329 that we adopt here are the Ripley's K function (Ripley, 1976) and the variogram (Cressie
 330 & Hawkins, 1980; Oliver & Webster, 2015).

331 2.3.1 Ripley's K Function

We briefly review the definition and interpretation of the Ripley's K function here. Interested readers can refer to Ripley (1976) for more details. The Ripley's K function is a functional summary of the density of a point cloud at various scales. Consider a set

of points with coordinates $\{(x_i, y_i)\}_{i=1}^n$, which are all located within an area of size A . The Ripley's K function is a function of the scale parameter d , defined as

$$L(d) = \sqrt{\frac{A \sum_{i=1}^n \sum_{j=1, j \neq i}^n k_{i,j}}{\pi n(n-1)}}, \quad (1)$$

where $k_{i,j} = 1$ if point (x_i, y_i) and point (x_j, y_j) are within Euclidean distance d . Intuitively, the Ripley's K function calculates the proportion of pairs of points that are within distance d . Since d can take on any arbitrary value, the Ripley's K function reflects the clustering and dispersion properties of the points in the point cloud.

The area size A is an important parameter in the calculation. In Figure 5 (a) and (b) we show two identical point clouds, generated from a 2D uniform distribution, located in areas of different sizes. In (a), the red bounding box shows the area considered when calculating the Ripley's K function for the point cloud. In (b), the area is the whole region: $[0, 20] \times [0, 20]$. With the same point cloud, one can see that their Ripley's K function, plotted in (d), are very different. The Ripley's K function for pattern A and B are relatively straight, meaning that points are nearly uniformly and randomly distributed in the area. When all points are randomly distributed, the proportion of points within radius d grows linearly with the size the circle πd^2 , so $L(d) \sim O(d)$ and the slope is related to \sqrt{A} . In Figure 5 (c), we show another point pattern coming from a Gaussian mixture distribution. Its corresponding Ripley's K function is plotted in (d) in green. With a relatively small d , the Ripley's K function is concave and indicates a clustering pattern of points. As d becomes larger, the function becomes convex and indicates that at a relatively large scale, distribution of points are dispersed (scattered in five clusters).

We need to define two key elements in order to calculate the Ripley's K function that contains the spatial information we desire from the SHARP parameter maps: an area and a point cloud within the area. In our implementation, we take the PIL region, as the area, and the number of pixels of the PIL region as the size A . Within the PIL region, we select all pixels with $|B_r|$ above a threshold τ . In some active regions, there are many pixels with extremely large $|B_r|$ values, leading to many pixels being selected above the threshold τ .

Based on the formula of Ripley's K function, one can see that it involves the pairwise distance matrix of all points. Empirically, we found that having over 500 points in the point cloud would make the computation of Ripley's K very time consuming. Therefore, if there are more than 500 such pixels, we randomly select only 500 of them where the probability of each pixel getting selected is proportional to $|B_r|$. When there are fewer than 500 pixels before the sub-sampling, we also sample with replacement to make the final point clouds having 500 points.

The pixels selected are the point clouds and their (x, y) coordinates in the B_r image specify their locations. The distance between any two pixels is the Euclidean distance between their coordinates. Since we are using the Cylindrical Equal Area (CEA) version of the B_r magnetogram, each pixel has the same physical size, so it makes sense to use the pixel coordinate instead of the true latitude and longitude as the pixel location.

In Figure 6, we show the point clouds generated with thresholds being 400G, 1000G and 1600G (on the left, middle, right columns) for the B_r component collected 1 hour prior to an M flare of HARP 377, without any sub-sampling for comparison purpose. The bottom row gives the corresponding Ripley's K functions for all pixel distances within the range $[0, 100]$. As we increase the threshold value τ , the point clouds are more and more clustered into several small clusters, and the Ripley's K function deviates more from a straight line (straight line corresponds to a random distribution pattern) towards the

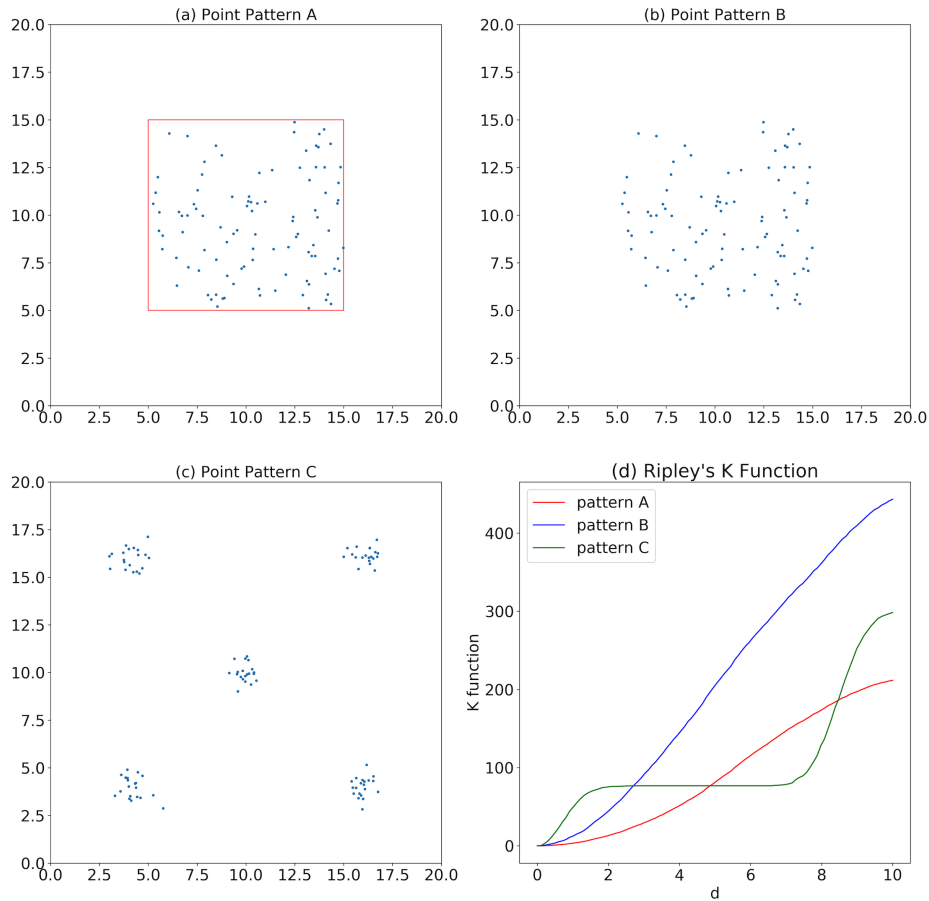


Figure 5. Schematic examples of Ripley's K function. (a) a uniformly distributed point cloud in a small area. (b) same point cloud but in a larger area, looking more like clustered in the middle. (c) a non-uniform point cloud. (d) Ripley's K function for all three point patterns. The function is nearly a straight line for both pattern A and B, indicating that points are uniformly randomly distributed in the area. But the different area sizes drastically scale the level of the function. Concave function indicates that points are more clustered than random while convex function indicates that points are more dispersed than random.

377
378

line pattern indicating a clustering pattern of points at various scales. This is exemplified also in the top row of Figure 6.

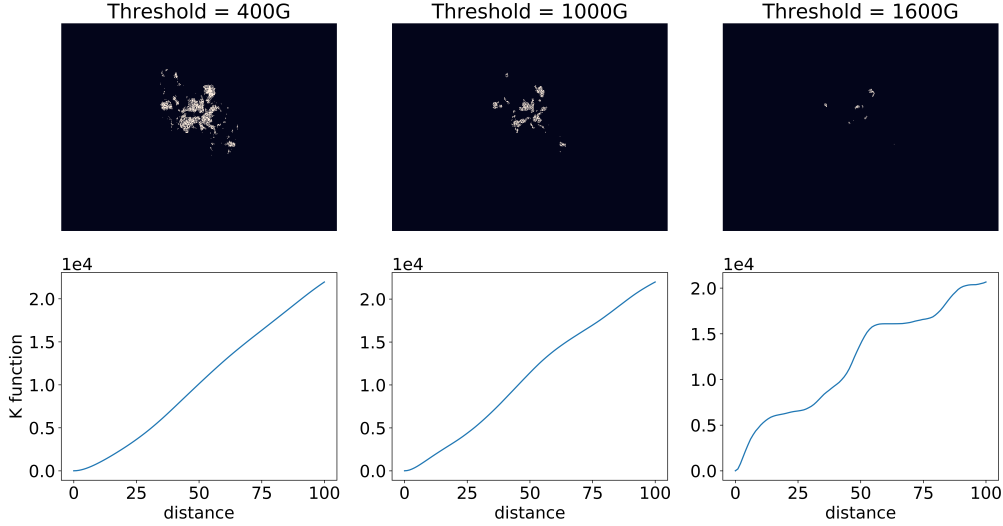


Figure 6. Point cloud and the corresponding Ripley's K function for the B_r component collected from HARP 377, 1 hour before the M flare peaked at 2011.02.13 17:38:00. The top row includes 3 point clouds generated by 3 thresholds at 400G, 1000G, 1600G. The bottom row shows the 3 corresponding Ripley's K functions.

379
380
381
382
383

Similar to the topological features, the Ripley's K function also locates the clusters of high B_r pixels. What sets it apart from the topological features is that it indicates at which scale (in terms of pixel distance) the clusters appear. In other words, the Ripley's K function provides additional information of the size of the loops, whereas topological features only captures the numbers of the loops.

384
385
386
387
388
389
390

In practice, we implement the Ripley's K function calculations for the B_r component as follows. For every B_r map, we use 11 thresholds at 0G, 200G, 400G, 600G, 800G, 1000G, 1200G, 1400G, 1600G, 1800G, 2000G, for generating the point clouds. We choose these thresholds because they can filter high $|B_r|$ value pixels at various magnitudes. There are some considerable differences among the point clouds selected based on these thresholds so that different Ripley's K functions do not have too much overlapping information.

391
392
393
394
395
396
397
398
399
400

For every point cloud, we calculate the Ripley's K function and evaluate the function on the distance grid $\{1, 2, \dots, 99, 100\}$. We restrict the upper bound of the distance scale at 100 (pixel scale) to guarantee that it works for all B_r images. Additionally, most PIL regions do not exceed 25,000 pixels, so analyzing a neighborhood of radius 100 for every pixel covers a sub-region large enough to within the PIL region for a meaningful sample while still remaining localized. Thus in total we have 11 Ripley's K functions and each function has 100 functional values, leading to 1,100 raw features per B_r map. When constructing the final feature, **we divide all Ripley's K functions by the number of PIL pixels**, namely A , so finally the level of Ripley's K function is inversely proportional to \sqrt{A} .

401

2.3.2 Variogram

Both the topological features and the Ripley's K function on the B_r maps are aimed at analyzing the clustering patterns of high $|B_r|$ pixels. Here we introduce another spatial statistics quantity, called the *variogram*, which is a description of the spatial continuity of the data. The variogram of the B_r map is a functional summary of the spatial variation of B_r at various scales. Again, we briefly introduce the definition and interpretations here, and interested readers shall refer to Omre (1984) for details. For any point cloud $(x_i, y_i)_{i=1}^n$, denote their B_r values as $z(x_i, y_i)$. At (Euclidean) distance d , the variogram is defined as

$$\gamma(d) = \gamma(\mathbf{s}_i, \mathbf{s}_j) = \frac{1}{2} \text{Var}[z(\mathbf{s}_i) - z(\mathbf{s}_j)], \quad (2)$$

402

403

where $\mathbf{s}_i = (x_i, y_i)$, $\mathbf{s}_j = (x_j, y_j)$ are two arbitrary points in the point cloud that has a Euclidean distance d in-between, and Var denotes the variance of a random variable.

404

405

406

407

408

409

410

411

412

The variogram measures the variance of the differences of B_r values between any two arbitrary pixels that have a distance d in between. The variogram is similar to the structure function, which has been applied to active regions to measure the fragmented nature of the magnetic network and its relationship to flares (Uritsky & Davila, 2012). In the B_r map, typically one would expect that when two pixels are close, their B_r values should be more similar. When two pixels are getting more distant, their B_r values can be more different as well. The relationship of local similarity and correlation of B_r and the scale d is captured by the variogram, which can provide extra spatial information on top of the topological features and the Ripley's K function.

413

414

415

416

417

418

419

In practice, it is hard to find a large number of pairs of pixels that are separated exactly by distance d . To estimate the empirical variogram, one would set a few disjoint bins of distance, and any pair of pixels would fall into one of the bins, depending on their distance. The variance is then calculated for all pairs of pixels belonging to the same bin. In our implementation of the variogram, we use the same point cloud for Ripley's K function calculation. In Figure 7, we show the corresponding variogram for the 3 point clouds shown in Figure 6.

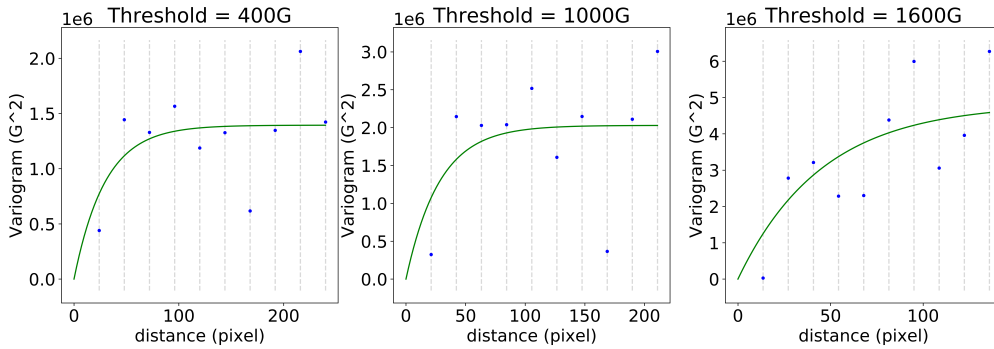


Figure 7. Variogram estimates for point clouds in Figure 6. Vertical dashed lines show the center of each distance interval, and the scatter points are the semi-variance (see equation 2) of B_r values for all pairs of pixels separated by the distance within the interval. The green line is the fitted curve for the variogram estimates (i.e. the scattered points). Note that the scales of x,y axes are different across the three graphs with distinct thresholds.

420

421

In each variogram, there are multiple distance bins whose centers are indicated by a vertical dashed line. In each bin, there are many pairs of pixels whose distance lies in

the distance bin. The scatter points are the variogram estimates based on all pairs of pixels in the same bin. The blue line is the fitted curve of the scatter points using an exponential parametric model:

$$\gamma(d|C_0, a) = C_0 \left(1 - e^{-\frac{d}{a}}\right) \quad (3)$$

Since different point clouds may have all sorts of pairs of pixels whose distance may vary in a wide range. Different variograms can have different distance bins, making it hard to vectorize the variogram as a fixed-length feature vector. As a partial solution, we fit the exponential parametric model above with least-squares and take the fitted parameter C_0, a for each variogram as its features. The two parameters C_0, a are termed as the sill and range parameter of the variogram. Since we have 11 point clouds per B_r map, and each variogram has 2 parameters, we have 22 variogram features for a single B_r map.

2.4 Feature Set Summary

In our feature construction, we use tools from TDA and Spatial Statistics to analyze the spatial distribution of SHARP parameters. For every flare, we first derive its nine SHARP parameter maps (Table 1). For each magnetogram, we detect the active region polarity inversion line (PIL) region and focus only on the PIL region for feature construction. Topology features are derived for all nine SHARP parameter maps, and each map has 19 Betti numbers counting the numbers of loops in the 19 bitmaps. Ripley's K function is applied to the B_r map only and every B_r map has 11 Ripley's K functions out of 11 thresholds, and every function is evaluated on a 100-point grid, leading to 1100 Ripley's K features. Variogram is also applied only to the B_r map and 11 variograms are calculated based on 11 thresholds, where each variogram only retains its sill and range parameter as features.

In addition to all these features, there are some extra features that do not belong to any of the categories above, so we group all of them, including the width and height of the B_r map, the size of the PIL region and the sum of PIL weights, as the auxiliary features. Figure 8 shows a workflow summary of all features constructed. The topology features and Ripley's K functions have high dimensions as shown in Figure 8, so we also use principal component analysis (PCA) and functional principal component analysis (FPCA) to reduce their dimensions. And we use the reduced dimensions as features for classification tasks. See the next section for details of the data preparation for prediction models.

3 Data Description and Prediction Results

In this section, we first introduce the dataset used for feature construction. Then we elaborate on the model we use for flare classification and the data pre-processing steps for dimension reductions on the feature sets. Finally, we demonstrate the prediction performances of different combinations of features and show the extra prediction gains of using topological and spatial statistics features on flare classification.

3.1 Description of Data

We use the Geostationary Operational Environmental Satellites (GOES) flare list spanning 2010/12 - 2018/06 for collecting flare events. There are originally 11,348 flares within this time range. For the purpose of flare classification, we only keep all B (weak), and M/X (strong) class flares. For each flare, we collect its corresponding high-resolution HMI magnetogram data from the JSOC at 4 time points: 1, 6, 12, 24 hours prior to the

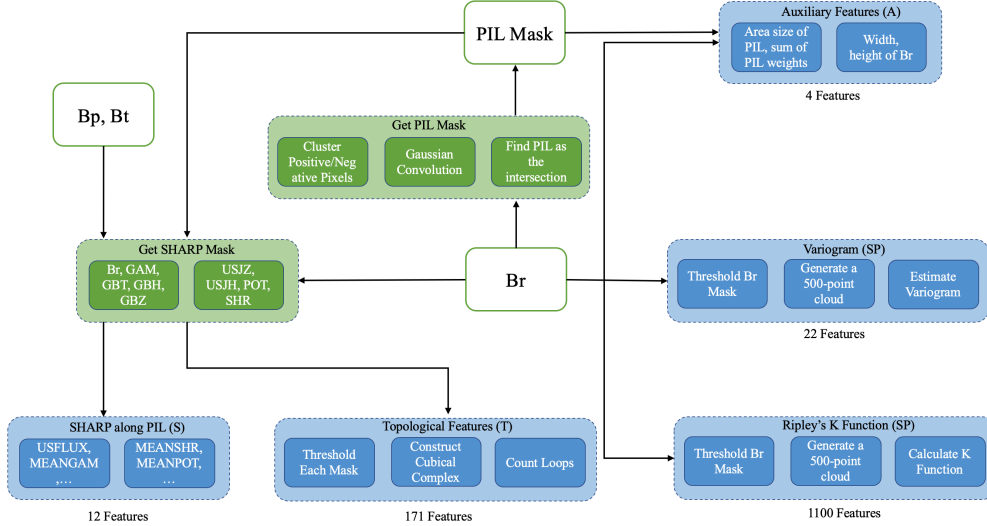


Figure 8. A Workflow Illustration of Feature Construction. The workflow chart shows all 5 sets of features constructed based on the HMI magnetograms. All source data and data used in the intermediate steps are colored in green and all output features are in blue. Small oval boxes include either the names of the features/masks or the steps for deriving the features/masks. Both of the topological features and Ripley’s K function have rather high dimensions, so we apply dimension-reduction procedures to compress information before inputting them into the flare classification model.

466 peak soft X-ray flux. These 4 time points lead to 4 datasets, and we perform feature con-
 467 struction and flare classifications separately for each of the 4 datasets.

468 Some of the flares do not have available data for all 4 time points, especially for
 469 12-hour and 24-hour data due to the lack of records at exactly 12 or 24 hours before the
 470 flare peak time, so we drop them to make sure that every flare appears in all four datasets,
 471 for sake of fair comparison across the four datasets. Finally, we have 399 M/X class flares
 472 and 1,972 B class flares coming from 487 HARP regions in each of the 4 datasets.

473 3.2 Data Pre-processing & Model Training

474 The prediction task is to classify strong (M/X) from weak (B) flares. For binary
 475 classification, we use the XGBoost model (T. Chen & Guestrin, 2016), which is an ef-
 476 ficient gradient boosting (Friedman, 2002) method with a decision tree (Safavian & Land-
 477 grebe, 1991) base learner. The XGBoost model is implemented using the *xgboost* pack-
 478 age in R, with the maximum depth of a tree set to 2, the learning rate set to 1 and the
 479 maximum number of rounds of boosting to be 100. We do not tune the parameter to op-
 480 timize the performances to leave a fair ground for the comparison of features. We train
 481 the model with several different combinations of features from the feature set detailed
 482 in Figure 8.

483 For topological features (**T**) and the Ripley’s K function features (**Ripley_K**), we
 484 have very high dimensional feature spaces. To efficiently compress the information, we
 485 conduct dimension reduction on both sets of features. Specifically, for the 19 topology
 486 features of every SHARP map, we do a principal component analysis (PCA) and keep
 487 top 5 PCs in place of the original 19 features. We have confirmed that by choosing the
 488 top 5 PCs, we are able to explain 97.67% ~ 99.61% variation of the topology features,

489 depending on the SHARP masks. For every Ripley’s K function, which is itself 100-dimensional,
 490 we carry out a functional principal component analysis (FPCA, Hall, Müller, and Wang
 491 (2006)) and keep top 5 PCs in place of the original 100 features. We can also confirm
 492 that the choice of top 5 PCs is able to summarize > 99% of the functional variation for
 493 each Ripley’s K function across all samples. After both steps, we reduce the topologi-
 494 cal features from 171 to 45 dimensions, and the Ripley’s K function features from 1100
 495 to 55 dimensions. We denote these dimension reduced features as **T_PC** (for topologi-
 496 cal features) and **Ripley_K_PC**, and the spatial statistics feature category as **SP_PC**,
 497 which includes the Ripley’s K principal components and the original variogram param-
 498 eter estimates.

499 To construct train and test sets for training and validating the classification model,
 500 we split the entire flare list according to their HARP regions. As a result, a flare from
 501 any HARP region appears in either train or test set only. On average, 70% of the HARP
 502 regions are assigned to the train set and the rest, 30%, go to the test set. The dimen-
 503 sion reduction of topological and Ripley’s K features are performed using the train set
 504 only and the test set PCs are predicted using the PCA and FPCA results from the train
 505 set. Other features are standardized based on the mean and standard deviation of the
 506 train set only to avoid information leaking.

507 There is randomness in the process of deriving the spatial statistics features be-
 508 cause we always randomly pick a point cloud with 500 points from all candidate pixels.
 509 To guarantee the robustness of the features derived, we re-run the derivation of all these
 510 features 10 times and take the average as the final features. To make the feature com-
 511 parison more robust to different train/test split, we re-run the model training/testing
 512 procedure 20 times, each time with a different train-test split, and then take the aver-
 513 age performance for feature comparison. The model is trained separately for the 4 datasets,
 514 but the flares in the train/test set, in each iteration, is the same for all 4 datasets.

515 3.3 Model Evaluation and Discussion

516 To compare the discriminating power of different sets of features in the flare clas-
 517 sification task, we define the M/X flares as the positive class and the B flares as the neg-
 518 ative class. We use the test set True Skill Score (TSS), as the benchmark defined as fol-
 519 lows:

$$\text{TSS} = \frac{\text{TP}}{\text{TP} + \text{FN}} - \frac{\text{FP}}{\text{FP} + \text{TN}},$$

520 where TP, TN are the positive (M/X), negative (B) samples that are classified cor-
 521 rectly, and FP, FN are the negative (B), positive (M/X) samples that are classified wrongly
 522 as being positive and negative, respectively. The range of TSS is from -1 to 1, and it is
 523 designed such that a random classifier or an unskilled classifier (always predicting the
 524 majority class) has TSS 0. In Table 2, we show the mean test-set TSS for different fea-
 525 ture sets across 20 iterations. In the Appendix, we include three extra tables for read-
 526 ers’ references. In Table A.1, we show the TSS with the same sets of features but trained
 527 with a totally random train-test split procedure. In Table A.2, we also show the mean
 528 test-set TSS with the same sets of features for a strong (M/X) vs. weak (B/C) flare clas-
 529 sification task. In Table A.3, we show the Heidke Skill Score (HSS) for the binary clas-
 530 sification (M/X vs. B) models.

Feature Combination	Prediction Time (hour)			
	1	6	12	24
S	0.553 (0.075)	0.555 (0.071)	0.539 (0.068)	0.489 (0.077)
T	0.548 (0.069)	0.575 (0.071)	0.561 (0.063)	0.525 (0.069)
SP	0.558 (0.066)	0.578 (0.076)	0.546 (0.071)	0.528 (0.072)
S+T	0.578 (0.071)	0.581 (0.072)	0.554 (0.057)	0.536 (0.052)
S+SP	0.56 (0.059)	0.58 (0.073)	0.538 (0.078)	0.533 (0.074)
S+T+SP	0.586 (0.077)	0.599 (0.068)	0.558 (0.08)	0.57 (0.06)
S+T_PC+SP_PC	0.554 (0.075)	0.561 (0.077)	0.53 (0.082)	0.533 (0.076)
S+T+SP+A	0.587 (0.071)	0.605 (0.063)	0.551 (0.077)	0.55 (0.059)
S+T_PC+SP_PC+A	0.578 (0.068)	0.561 (0.071)	0.533 (0.076)	0.521 (0.089)

Table 2. Average True Skill Score (TSS), based on 20 train-test splits, for classifying strong (M/X) vs. weak (B) flares using different sets of features. Standard errors calculated based on a bootstrap procedure are given in brackets. Feature shorthand represents: SHARP parameter (**S**); Topology feature (**T**); Spatial Statistics feature (**SP**); Auxiliary feature (**A**); Topology feature principal component score (**T_PC**); Spatial statistics with functional principal component score for Ripley’s K function (**SP_PC**). Boldface numbers indicate that the TSS is significantly higher than the benchmark model (**S**), which is fitted only with PIL-weighted SHARP parameters, across the 20 iterations. The column names labeled by 1,6,12,24 stands for the 4 datasets collected at 1,6,12,24 hours before the flare peak time.

531 We define the model fitted with SHARP parameters as the benchmark model, and
532 compare all other feature combinations against it. We can see the average TSS differ-
533 ences between some combinations of features against the benchmark. To formally test
534 whether such TSS differences are significant, we apply a one-sided paired Student’s t-
535 test to test the null hypothesis that a certain feature combination has the same TSS as
536 the benchmark for any arbitrary train-test split. In Table ??, we highlight the TSS in
537 boldface when the TSS of a certain feature combination is significantly higher than the
538 benchmark, i.e. we reject the null hypothesis with 95% confidence. Since the sample size
539 is small and we split the train and test set based on HARP regions, the uncertainty can
540 be large. Given the high uncertainty of the TSS for every feature set, it is more infor-
541 mative to look at the pairwise hypothesis testing result (pairing TSS score based on each

train/test split), which suggests the presence of performance improvement when adding new features.

As one can see that when using the topological and spatial statistics features, we can improve the TSS of flare classification 12-24 hours before the flare peak time, and further improves when it is getting close to the flare peak time (i.e. 1,6 hours before). When combining all features together, we can do significantly better than only using the SHARP parameters. When we reduce the dimension of the topological and spatial statistics features, we can still maintain a margin of skill improvement in the 24 hour prediction time scenario. The improvement is even more salient for the Heidke Skill Score, as shown in Table A.3.

Different from our topological features, in Deshmukh, Berger, Bradley, and Meiss (2020); Deshmukh, Berger, Meiss, and Bradley (2020), the authors split the B_r mask into a positive component and a negative component and calculate the Betti numbers separately for the two components. We tried the same method and replace the topology features of the B_r channel with two sets of features corresponding to its positive/negative component but did not get any significantly different results. We contemplate that the reasons are: 1) other SHARP masks have taken the sign of flux into account; 2) the feature space is very high-dimensional. So we still stick to our original topology features when we report our results.

As discussed in Barnes et al. (2016) and subsequent related works on flare forecasting, it is impossible or unfair to compare skill scores directly with published work in literature when the data preparation procedures are conducted differently. The same story goes for our case here. However, with the same data preparation adopted for various prediction models that we train and test, the conclusions that we make within the scope of this paper are based on fair comparisons. Our ultimate goal of this work is not to give the “best” prediction model for solar flare events, but to construct and interpret meaningful features that are useful for flare forecasting. Interested readers can refer to Barnes et al. (2016), Leka et al. (2019a), and X. Wang et al. (2020) for more thorough comparisons of results for flare forecasting models published in literature.

The performance improvement introduced by the new features is incremental and significant based on our significance testing results. Besides measuring the contribution of all new features using the TSS, we also calculate the individual feature importance using the Fisher score (F-score (Stork et al., 2001), as adopted by Bobra et al. (2014); Deshmukh, Berger, Bradley, and Meiss (2020)). The Fisher score measures the individual feature’s discriminating power in a binary classification setting. For any feature, x_i , the Fisher score is calculated as

$$F(i) = \frac{(\bar{x}_i^+ - \bar{x}_i)^2 + (\bar{x}_i^- - \bar{x}_i)^2}{\frac{1}{n^+ - 1} \sum_{k=1}^{n^+} (x_{k,i}^+ - \bar{x}_i)^2 + \frac{1}{n^- - 1} \sum_{k=1}^{n^-} (x_{k,i}^- - \bar{x}_i)^2},$$

where \bar{x}_i^+ , \bar{x}_i^- are the subgroup mean of x_i for all positive, negative samples; n^+ , n^- are the numbers of positive, negative samples; and $x_{k,i}^+$, $x_{k,i}^-$ are the k -th observation of the positive, negative class. The Fisher score is the ratio of between-class variation and within-class variation. A high Fisher score indicates that the feature shows high separability for the two classes. We rank all features including the SHARP parameters (**S**), topological feature principal component scores (**T_PC**), Ripley’s K functional principal component scores (**Ripley_K_PC**), variogram (**V-gram**) and auxiliary features (**A**) based on their F-score, for the 4 datasets separately. All scores are calculated using the full dataset. In Figure 9, we show the top 15 features in their order of F-score (normalized to range [0, 1]), and color them based on their feature categories.

The feature ranking shows that the newly constructed features have equally good or even better individual discriminating power than the SHARP parameters. Among all

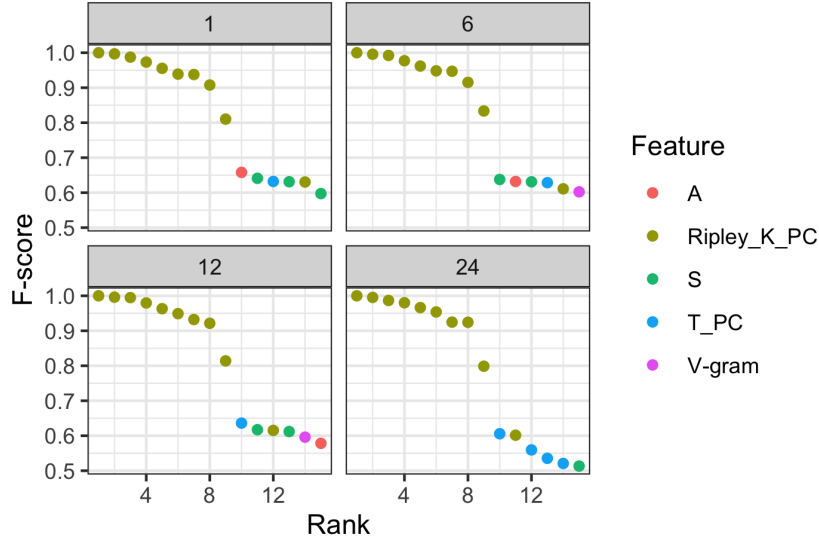


Figure 9. Normalized Fisher Score for selected features. Four panels correspond to the 1,6,12,24 hour dataset. In each panel, top 15 features in terms of F-score are plotted. Among all 4 datasets, the top features are always the Ripley’s K function’s principal component score. Some features from other categories also rank among the top 15 features. The F-score ranking indicates that the spatial statistics features, especially the Ripley’s K function, have greater individual discriminating power compared to SHARP parameters.

new features, the Ripley’s K function stands out as the features with the highest discriminating power. Specifically, the top features are the 1st PC score of Ripley’s K function generated based on different threshold values.

To visualize the discriminating power of Ripley’s K function, we choose four representative cases, two for B flare and two for M flare, and show their B_r , PIL mask, sampled point cloud at threshold 2000G and the corresponding Ripley’s K function (divided by the number of PIL pixels) in Figure 10. The most distinctive difference between the derived Ripley’s K functions, as one can see by comparing the four plots, is the level of the function value. There are two factors that create the level difference: PIL area size and concentration of high- B_r pixels. Since we divide each function by the number of PIL pixels, the function value tends to be small when the PIL area is large. The B flare examples have longer, wide-spread PIL regions, as suggested by the PIL mask, but only have small scattered pieces of high- B_r regions along the PIL. Both of these facts would lead to a low functional value. The M flares, on the contrary, have smaller PIL areas, but the high- B_r regions are close to each other and clustered into relatively bigger chunks. Both of these lead to higher functional values.

Apart from the differences of the level of the functions, one may also notice that the shape of the functions differ. The B flares have two jumps in the function while the M flares have a constantly increasing trend prior to the plateau. This exactly corresponds to the scattered small pieces of high- B_r regions shown in both B flare cases. Possibly some of the scattered small clusters of high- B_r pixels for the B flare locate outside of the flaring area. The functions for the M flare have an increasing trend overall, suggesting that there is a region full of high- B_r pixels (i.e. there are such pairs of high-flux pixels separated by an arbitrary distance within range $0 \sim 80$). The flare discriminator, captured by the Ripley’s K function, is essentially the degree of concentration of high-flux regions

615 of an active region, along the polarity inversion line. An M-flare tends to have a larger
 616 proportion of high-flux B_r pixels clustered spatially in the flaring area, leading to a dif-
 617 ferent Ripley's K function in terms of both functional level and shape, as compared to
 618 a B-flare.

619 The variogram effective range parameters also differ significantly between the B
 620 and M flares. For instance, the variogram of the B flare from HARP 1638 has a range
 621 parameter at 1.96 while the M flare from HARP 3311 has it at 75.95. This fact suggests
 622 that most of the B_r spatial variations are observed within ~ 2 pixel distances for the
 623 B flare point cloud and ~ 76 pixel distances for the M flare point cloud. This further
 624 consolidates our argument that the B flare has small, scattered clusters of pixels with
 625 high B_r values but the M flare has larger concentrations of such pixels.

626 In conclusion, the spatial statistics features we derived tend to predict an onset of
 627 a strong flare when observing the following B_r pattern: 1) small PIL area; 2) large clus-
 628 ters of high- B_r pixels not locating far from each other; 3) large B_r value variation be-
 629 tween clusters (e.g. between clusters of strongly positive and strongly negative flux). Such
 630 a pattern is not exhaustive for all strong flares, but it covers the majority of the cases
 631 and leads to features with high discriminating power.

632 4 Conclusion

633 In this paper, we investigate new features, on top of the SHARP parameters, for
 634 flare classification task. The first set of features is derived from persistence homology in
 635 topological data analysis, following the idea in Deshmukh, Berger, Meiss, and Bradley
 636 (2020). We extend the scope of HMI images from just the B_r component to multiple SHARP
 637 parameter maps when conducting the analysis, and pay specific attention to the polar-
 638 ity inversion line region (PIL). The second set of features come from spatial statistics
 639 concepts. The Ripley's K function analyzes the spatial clustering/dispersion patterns of
 640 pixels with high B_r . The Variogram analyzes the spatial variation of the B_r flux at var-
 641 ious distance scales. Both sets of features summarize some information regarding the spa-
 642 tial distribution of SHARP parameters, which adds additional information to the fea-
 643 ture set that SHARP parameters themselves cannot provide. We demonstrate how the
 644 new features can improve skills of the prediction model and also show that new features,
 645 especially the Ripley's K functions, have great discriminating power.

646 One major finding, besides the prediction performance gains, is that by focusing
 647 on the B_r component only, one can still derive topological and spatial features that has
 648 equal or superior predictive power than the SHARP parameters. We find that the top
 649 features for discrimination are the Ripley's K functions based on the B_r component and
 650 topological features of the B_r component. This result suggests that the spatial and shape
 651 information we derived from the B_r component alone is a more powerful discriminator
 652 than the SHARP quantities derived from the horizontal magnetic field components. One
 653 of our future research goals is to analyze the spatial correlations of the B_r component
 654 and the other SHARP quantities and check if there are systematic differences across dif-
 655 ferent classes of solar flares.

656 We note that our findings of a strong correlation between the B_r spatial distribu-
 657 tion and the flare productivity shows an inherent connection between the free energy buildup
 658 and release in solar flares that is related to the clustering and proximity of flux to the
 659 PIL. Such a connection has been established earlier by (Falconer et al., 2003) and (Schrijver
 660 et al., 2005; Schrijver, 2007) who respectively found the gradient and proximity of the
 661 magnetic flux (line-of-sight component) with respect to the PIL to be strongly correlated
 662 with flares and coronal mass ejections. Our work goes much further in establishing this
 663 relationship to such a degree that it has greater discriminating power for solar flares than
 664 the SHARP parameters derived from the full vector magnetic field.

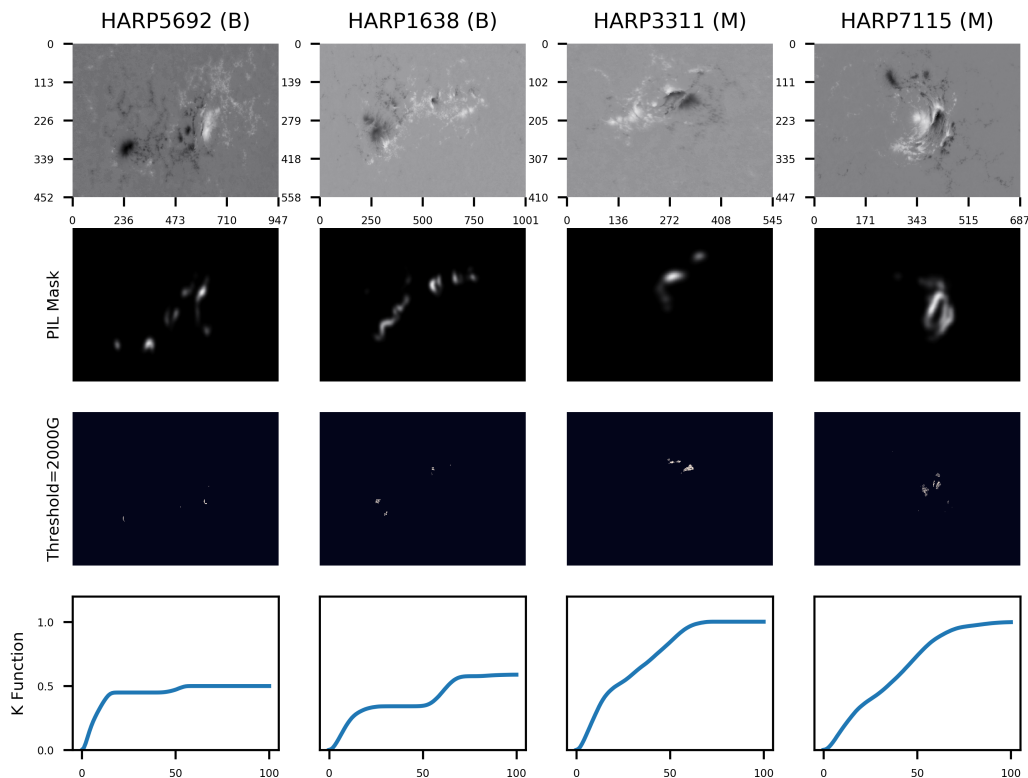


Figure 10. Four flare examples (columns 1-4): B6.1 from HARP 5692 peaked at 04:36, Jun 26, 2015; B5.3 from HARP 1638 peaked at 02:23, May 09, 2012; M1.0 from HARP 3311 peaked at 19:53, Oct 26, 2013; M1.0 from HARP 7115 peaked at 03:51, Sept 05, 2017. The four rows correspond to their B_r values, PIL masks, point clouds with $B_r > 2000$ G within each PIL region, and the Ripley's K functions respectively. The K function differs, in terms of level and shape, between two M flares and two B flares. The main reason is that there are only scattered small clusters of high- B_r regions for the B flares. On the contrary, M flares have a sub-region full of high- B_r pixels.

665 From a theoretical perspective, our work suggest that the necessary components
 666 for flares, complexity and also free energy are intrinsically related to one another through
 667 the photospheric B_r distribution. The relationship to B_r and coronal free energy is not
 668 immediately obvious. However, we may infer that the energized coronal field may result
 669 from the evolution of non-force-free fields in the convection zone that produce signatures
 670 in the B_r distribution detected by our statistical analysis. Such forces may affect the way
 671 individual flux tubes find cohesion from magnetic twist or emerge through the convec-
 672 tion zone. A physical basis for this conjecture is found in simulations of flux emergence
 673 of kink-unstable flux ropes that form delta spots, which are highly prone to flaring (Linton
 674 et al., 1998; Fang & Fan, 2015; Toriumi & Hotta, 2019). Simulations of flux emergence
 675 also show the development of strong shear along forming PILs (Manchester, 2001; Fan,
 676 2001; Manchester, 2007; Archontis & Török, 2008; Fang et al., 2010; Török et al., 2014),
 677 as well as producing eruptive behavior (Manchester et al., 2004). Our spatial and topo-
 678 logical analysis suggest a more subtle and universal process may be at work developing
 679 the photospheric magnetic field and coronal free energy in a related way.

680 The analysis of the B_r component at multiple thresholds and multiple spatial scales
 681 can also be found in the thread of research on the fractal dimensions of flaring areas (Aschwanden
 682 et al., 2016; Aschwanden & Aschwanden, 2008; McAteer et al., 2005). They found that
 683 typically M/X flares have higher 2D fractal dimensions, indicating a larger flaring ar-
 684 eas of high B_r . The key difference between the spatial statistics tools we adopted and
 685 the fractal dimensions is that, after we choose B_r areas above a threshold, we measure
 686 the spatial clustering pattern of high B_r pixels, rather than the size of the area, since
 687 we always randomly sample 500 pixels in the high flux areas for analysis. We do believe
 688 that our work complements the researches on fractal dimensions to further quantify the
 689 shape complexity of strong B_r areas at multiple scales, and our result suggests that there
 690 are more discriminating features to be found in the shape (i.e. clustering pattern) of the
 691 strong B_r areas, beyond their size.

692 With this paper, we also want to popularize the application of spatial statistics tools,
 693 which can provide both interpretable and predictive features for various machine learn-
 694 ing tasks. The biggest advantage of the Ripley's K function and Variogram in our pa-
 695 per is that they can summarize the spatial patterns at various scales and give functional
 696 summary of the spatial distributions of the physical quantities. Focusing on various spa-
 697 tial scales can potentially uncover the multi-level patterns that are relevant for the ini-
 698 tiation of flares. In the future, we want to apply the same or similar tools to analyze not
 699 just snapshots of HARP regions, but time-series of HARP regions magnetograms to see
 700 if there are temporal trends of such spatial information that can further benefit flare pre-
 701 dictions.

702 Acknowledgments

703 All codes and data are included in our Github repository at [https://github.com/husun0822/
 704 spat_feature_flare_pred](https://github.com/husun0822/spat_feature_flare_pred). This work is supported by NASA grant 80NSSC20K0600,
 705 NSF DMS 1811083. W. Manchester is also supported by NASA grant 80NSSC18K1208.

706 References

- 707 Archontis, V., & Török, T. (2008, December). Eruption of magnetic flux ropes dur-
 708 ing flux emergence. *Astronomy and Astrophysics*, *492*, L35-L38. doi: 10.1051/
 709 0004-6361:200811131
- 710 Aschwanden, M. J., & Aschwanden, P. D. (2008). Solar flare geometries. i. the area
 711 fractal dimension. *The Astrophysical Journal*, *674*(1), 530.
- 712 Aschwanden, M. J., Crosby, N. B., Dimitropoulou, M., Georgoulis, M. K., Her-
 713 garten, S., McAteer, J., ... Uritsky, V. (2016). 25 years of self-organized
 714 criticality: solar and astrophysics. *Space Science Reviews*, *198*(1), 47–166.
- 715 Barnes, G., Leka, K., Schumer, E., & Della-Rose, D. (2007). Probabilistic forecasting
 716 of solar flares from vector magnetogram data. *Space Weather*, *5*(9).
- 717 Barnes, G., Leka, K. D., Schrijver, C. J., Colak, T., Qahwaji, R., Ashamari, O., ...
 718 Higgins, P. (2016). A comparison of flare forecasting methods. i. results from
 719 the all-clear workshop. *The Astrophysical Journal*, *829*(2), 89.
- 720 Bobra, M. G., & Couvidat, S. (2015). Solar flare prediction using SDO/HMI vec-
 721 tor magnetic field data with a machine-learning algorithm. *The Astrophysical
 722 Journal*, *798*(2), 135.
- 723 Bobra, M. G., Sun, X., Hoeksema, J. T., Turmon, M., Liu, Y., Hayashi, K., ...
 724 Leka, K. D. (2014, Sep 01). The helioseismic and magnetic imager (hmi) vec-
 725 tor magnetic field pipeline: Sharps – space-weather hmi active region patches.
 726 *Solar Physics*, *289*(9), 3549–3578.
- 727 Camporeale, E. (2019, jul). The challenge of machine learning in space weather now-
 728 casting and forecasting. *Space Weather*, *17*. doi: 10.1029/2018sw002061
- 729 Chen, T., & Guestrin, C. (2016). Xgboost: A scalable tree boosting system. In
 730 *Proceedings of the 22nd acm sigkdd international conference on knowledge*

- 731 *discovery and data mining* (pp. 785–794).
- 732 Chen, Y., Manchester, W. B., Hero, A. O., Toth, G., DuFumier, B., Zhou, T., . . .
- 733 Gombosi, T. I. (2019). Identifying solar flare precursors using time series of
- 734 sdo/hmi images and sharp parameters. *Space Weather*, *17*(10), 1404–1426.
- 735 Cressie, N., & Hawkins, D. M. (1980). Robust estimation of the variogram: I.
- 736 *Journal of the International Association for Mathematical Geology*, *12*(2),
- 737 115–125.
- 738 Deshmukh, V., Berger, T., Meiss, J., & Bradley, E. (2020). Shape-based feature en-
- 739 gineering for solar flare prediction. *arXiv preprint arXiv:2012.14405*.
- 740 Deshmukh, V., Berger, T. E., Bradley, E., & Meiss, J. D. (2020). Leveraging the
- 741 mathematics of shape for solar magnetic eruption prediction. *Journal of Space*
- 742 *Weather and Space Climate*, *10*, 13.
- 743 Ester, M., Kriegel, H.-P., Sander, J., & Xu, X. (1996). A density-based algorithm for
- 744 discovering clusters in large spatial databases with noise. In *Kdd* (Vol. 96, pp.
- 745 226–231).
- 746 Falconer, D. A. (2001, November). A prospective method for predicting coronal
- 747 mass ejections from vector magnetograms. *J. Geophys. Res.*, *106*, 25185–25190.
- 748 doi: 10.1029/2000JA004005
- 749 Falconer, D. A., Moore, R. L., & Gary, G. A. (2002, April). Correlation of the
- 750 Coronal Mass Ejection Productivity of Solar Active Regions with Measures of
- 751 Their Global Nonpotentiality from Vector Magnetograms: Baseline Results.
- 752 *Astrophys. J.*, *569*, 1016–1025. doi: 10.1086/339161
- 753 Falconer, D. A., Moore, R. L., & Gary, G. A. (2003, October). A measure from line-
- 754 of-sight magnetograms for prediction of coronal mass ejections. *J. Geophys.*
- 755 *Res.*, *108*, 1380. doi: 10.1029/2003JA010030
- 756 Falconer, D. A., Moore, R. L., & Gary, G. A. (2006, June). Magnetic Causes of So-
- 757 lar Coronal Mass Ejections: Dominance of the Free Magnetic Energy over the
- 758 Magnetic Twist Alone. *Astrophys. J.*, *644*, 1258–1272. doi: 10.1086/503699
- 759 Fan, Y. (2001, June). The Emergence of a Twisted Ω -Tube into the Solar Atmo-
- 760 sphere. *Astrophys. J. Lett.*, *554*, L111–L114. doi: 10.1086/320935
- 761 Fang, F., & Fan, Y. (2015, June). δ -Sunspot Formation in Simulation of Active-
- 762 region-scale Flux Emergence. *Astrophys. J.*, *806*(1), 79. doi: 10.1088/0004
- 763 -637X/806/1/79
- 764 Fang, F., Manchester, W., Abbett, W. P., & van der Holst, B. (2010, May). Simu-
- 765 lation of Flux Emergence from the Convection Zone to the Corona. *Astrophys.*
- 766 *J.*, *714*, 1649–1657. doi: 10.1088/0004-637X/714/2/1649
- 767 Florios, K., Kontogiannis, I., Park, S.-H., Guerra, J. A., Benvenuto, F., Bloomfield,
- 768 D. S., & Georgoulis, M. K. (2018). Forecasting solar flares using magnetogram-
- 769 based predictors and machine learning. *Solar Physics*, *293*(2), 28. doi:
- 770 doi:10.1007/s11207-018-1250-4
- 771 Friedman, J. H. (2002). Stochastic gradient boosting. *Computational statistics &*
- 772 *data analysis*, *38*(4), 367–378.
- 773 Gelfand, A. E., Diggle, P., Guttorp, P., & Fuentes, M. (2010). *Handbook of spatial*
- 774 *statistics*. CRC press.
- 775 Ghrist, R. (2008). Barcodes: the persistent topology of data. *Bulletin of the Ameri-*
- 776 *can Mathematical Society*, *45*(1), 61–75.
- 777 Hall, P., Müller, H.-G., & Wang, J.-L. (2006). Properties of principal component
- 778 methods for functional and longitudinal data analysis. *The annals of statistics*,
- 779 1493–1517.
- 780 Jiao, Z., Sun, H., Wang, X., Manchester, W., Gombosi, T., Hero, A., & Chen, Y.
- 781 (2020). Solar flare intensity prediction with machine learning models. *Space*
- 782 *Weather*, *18*(7), e2020SW002440.
- 783 Kaczynski, T., Mischaikow, K. M., & Mrozek, M. (2004). *Computational homology*
- 784 (Vol. 3) (No. 7). Springer.
- 785 Leka, K. D., & Barnes, G. (2003a, October). Photospheric Magnetic Field Proper-

- 786 ties of Flaring versus Flare-quiet Active Regions. I. Data, General Approach,
787 and Sample Results. *Astrophys. J.*, 595(2), 1277-1295. doi: 10.1086/377511
- 788 Leka, K. D., & Barnes, G. (2003b, October). Photospheric Magnetic Field Prop-
789 erties of Flaring versus Flare-quiet Active Regions. II. Discriminant Analysis.
790 *Astrophys. J.*, 595, 1296-1306. doi: 10.1086/377512
- 791 Leka, K. D., & Barnes, G. (2018). Solar flare forecasting: Present methods and chal-
792 lenges. In N. Buzulukova (Ed.), *Extreme events in geospace* (pp. 65 – 98). El-
793 sevier. doi: 10.1016/B978-0-12-812700-1.00003-0
- 794 Leka, K. D., Park, S.-H., Kusano, K., Andries, J., Barnes, G., Bingham, S., ...
795 Terkildsen, M. (2019a, aug). A comparison of flare forecasting methods. II.
796 benchmarks, metrics, and performance results for operational solar flare fore-
797 casting systems. *The Astrophysical Journal Supplement Series*, 243(2), 36.
798 Retrieved from <https://doi.org/10.3847/2F1538-4365%2Fab2e12> doi:
799 10.3847/1538-4365/ab2e12
- 800 Leka, K. D., Park, S.-H., Kusano, K., Andries, J., Barnes, G., Bingham, S., ...
801 Terkildsen, M. (2019b, aug). A comparison of flare forecasting methods.
802 III. systematic behaviors of operational solar flare forecasting systems. *The*
803 *Astrophysical Journal*, 881(2), 101. Retrieved from [https://doi.org/](https://doi.org/10.3847/2F1538-4357%2Fab2e11)
804 [10.3847/2F1538-4357%2Fab2e11](https://doi.org/10.3847/2F1538-4357%2Fab2e11) doi: 10.3847/1538-4357/ab2e11
- 805 Linton, M. G., Dahlburg, R. B., Fisher, G. H., & Longcope, D. W. (1998, Novem-
806 ber). Nonlinear Evolution of Kink-unstable Magnetic Flux Tubes and Solar δ -
807 Spot Active Regions. *Astrophys. J.*, 507(1), 404-416. doi: 10.1086/306299
- 808 Liu, C., Deng, N., Wang, J. T. L., & Wang, H. (2017, July). Predicting Solar Flares
809 Using SDO/HMI Vector Magnetic Data Products and the Random Forest
810 Algorithm. *Astrophys. J.*, 843(2), 104. doi: 10.3847/1538-4357/aa789b
- 811 Liu, H., Liu, C., Wang, J. T. L., & Wang, H. (2019, jun). Predicting solar flares
812 using a long short-term memory network. *The Astrophysical Journal*, 877(2),
813 121. Retrieved from <https://doi.org/10.3847/2F1538-4357%2Fab1b3c> doi:
814 10.3847/1538-4357/ab1b3c
- 815 Manchester, W., IV. (2001, January). The Role of Nonlinear Alfvén Waves in
816 Shear Formation during Solar Magnetic Flux Emergence. *Astrophys. J.*, 547,
817 503-519. doi: 10.1086/318342
- 818 Manchester, W., IV. (2007, September). Solar Atmospheric Dynamic Coupling
819 Due to Shear Motions Driven by the Lorentz Force. *Astrophys. J.*, 666, 532-
820 540. doi: 10.1086/520493
- 821 Manchester, W., IV, Gombosi, T., DeZeeuw, D., & Fan, Y. (2004, July). Eruption of
822 a Buoyantly Emerging Magnetic Flux Rope. *Astrophys. J.*, 610, 588-596. doi:
823 10.1086/421516
- 824 Maria, C., Boissonnat, J.-D., Glisse, M., & Yvinec, M. (2014). The gudhi library:
825 Simplicial complexes and persistent homology. In *International congress on*
826 *mathematical software* (pp. 167–174).
- 827 McAteer, R. J., Gallagher, P. T., & Ireland, J. (2005). Statistics of active region
828 complexity: A large-scale fractal dimension survey. *The Astrophysical Journal*,
829 631(1), 628.
- 830 Munch, E. (2017). A users guide to topological data analysis. *Journal of Learning*
831 *Analytics*, 4(2), 47–61.
- 832 Muranushi, Y. H., Muranushi, T., Asai, A., Okanohara, D., Raymond, R., Watan-
833 abe, G., ... Shibata, K. (2016). A deep-learning approach for operation of
834 an automated realtime flare forecast. *CoRR*, *abs/1606.01587*. Retrieved from
835 <http://arxiv.org/abs/1606.01587>
- 836 Nishizuka, N., Kubo, Y., Sugiura, K., Den, M., & Ishii, M. (2021). Operational solar
837 flare prediction model using deep flare net. *Earth, Planets and Space*, 73(1),
838 1–12.
- 839 Nishizuka, N., Sugiura, K., Kubo, Y., Den, M., & Ishii, M. (2018). Deep flare net
840 (defn) model for solar flare prediction. *The Astrophysical Journal*, 858(2),

841
842
843
844
845
846
847
848
849
850
851
852
853
854
855
856
857
858
859
860
861
862
863
864
865
866
867
868
869
870
871
872
873
874
875
876
877
878
879
880
881
882

- 113.
- Oliver, M. A., & Webster, R. (2015). *Basic steps in geostatistics: the variogram and kriging*. Springer.
- Omre, H. (1984). The variogram and its estimation. In *Geostatistics for natural resources characterization* (pp. 107–125). Springer.
- Ripley, B. D. (1976). The second-order analysis of stationary point processes. *Journal of applied probability*, *13*(2), 255–266.
- Safavian, S. R., & Landgrebe, D. (1991). A survey of decision tree classifier methodology. *IEEE transactions on systems, man, and cybernetics*, *21*(3), 660–674.
- Schrijver, C. J. (2007, jan). A characteristic magnetic field pattern associated with all major solar flares and its use in flare forecasting. *Astrophysical Journal*, *655*(2), L117–L120.
- Schrijver, C. J., De Rosa, M. L., Title, A. M., & Metcalf, T. R. (2005, July). The Nonpotentiality of Active-Region Coronae and the Dynamics of the Photospheric Magnetic Field. *Astrophys. J.*, *628*(1), 501–513. doi: 10.1086/430733
- Stork, D. G., Duda, R. O., Hart, P. E., & Stork, D. (2001). Pattern classification. *A Wiley-Interscience Publication*.
- Toriumi, S., & Hotta, H. (2019, November). Spontaneous Generation of δ -sunspots in Convective Magnetohydrodynamic Simulation of Magnetic Flux Emergence. *Astrophys. J. Lett.*, *886*(1), L21. doi: 10.3847/2041-8213/ab55e7
- Török, T., Leake, J. E., Titov, V. S., Archontis, V., Mikić, Z., Linton, M. G., ... Kliem, B. (2014, February). Distribution of Electric Currents in Solar Active Regions. *Astrophys. J. Lett.*, *782*, L10. doi: 10.1088/2041-8205/782/1/L10
- Uritsky, V. M., & Davila, J. M. (2012, March). Multiscale Dynamics of Solar Magnetic Structures. *Astrophys. J.*, *748*(1), 60. doi: 10.1088/0004-637X/748/1/60
- Wang, J., Liu, S., Ao, X., Zhang, Y., Wang, T., & Liu, Y. (2019, oct). Parameters derived from the SDO/HMI vector magnetic field data: Potential to improve machine-learning-based solar flare prediction models. *Astrophysical Journal*, *884*(2), 175.
- Wang, J., Zhang, Y., Webber, S. A. H., Liu, S., Meng, X., & Wang, T. (2020). Solar flare predictive features derived from polarity inversion line masks in active regions using an unsupervised machine learning algorithm. *The Astrophysical Journal*, *892*(2), 140.
- Wang, X., Chen, Y., Toth, G., Manchester, W. B., Gombosi, T. I., Hero, A. O., ... Liu, Y. (2020). Predicting solar flares with machine learning: investigating solar cycle dependence. *The Astrophysical Journal*, *895*(1), 3.
- Wasserman, L. (2018). Topological data analysis. *Annual Review of Statistics and Its Application*, *5*, 501–532.
- Zomorodian, A. J., et al. (2012). *Advances in applied and computational topology: American mathematical society short course on computational topology, january 4-5, 2011, new orleans, louisiana* (Vol. 70). American Mathematical Soc.

A Appendices

A.1 TSS based on random train-test split

Here are the results of TSS scores when we split train and test set randomly:

Feature Combination	Prediction Time (hour)			
	1	6	12	24
S	0.613 (0.033)	0.619 (0.04)	0.588 (0.046)	0.554 (0.037)
T	0.621 (0.041)	0.627 (0.037)	0.601 (0.038)	0.59 (0.05)
SP	0.606 (0.039)	0.642 (0.032)	0.587 (0.046)	0.593 (0.046)
S+T	0.647 (0.044)	0.653 (0.048)	0.612 (0.034)	0.587 (0.044)
S+SP	0.624 (0.03)	0.648 (0.033)	0.605 (0.032)	0.579 (0.039)
S+T+SP	0.647 (0.037)	0.66 (0.039)	0.625 (0.042)	0.608 (0.045)
S+T_PC+SP_PC	0.616 (0.036)	0.624 (0.048)	0.6 (0.054)	0.591 (0.039)
S+T+SP+A	0.665 (0.04)	0.66 (0.043)	0.64 (0.042)	0.615 (0.039)
S+T_PC+SP_PC+A	0.628 (0.046)	0.621 (0.043)	0.608 (0.046)	0.589 (0.043)

Table A.1. Average True Skill Score (TSS), based on 20 random train-test split, for classifying strong (M/X) vs. weak (B) flares using different sets of features. Standard error in brackets. Feature shorthand represents: SHARP parameter (**S**); Topology feature (**T**); Spatial Statistics feature (**SP**); Auxiliary feature (**A**); Topology feature principal component score (**T_PC**); Spatial statistics with functional principal component score for Ripley’s K function (**SP_PC**). Boldface numbers indicate that the TSS is significantly higher than the benchmark model (**S**), which is fitted only with SHARP parameters in the PIL region, across the 20 iterations. The column names labeled by 1,6,12,24 stands for the 4 datasets collected at 1,6,12,24 hours before the flare peak time.

886
887
888
889
890
891
892**A.2 TSS for M/X vs. B/C**

The following table shows the result of TSS scores when we classify M/X flares against B/C flares. The TSS, when compared to our main result in Table 2, is much lower due to the inclusion of C-class flares. But the area under curve (AUC) for all feature combinations remain at a high level at around 0.69 ~ 0.78 and the statistical significance is also consistent with our main result: the new features can improve on top of the SHARP parameters, especially when one wants to predict flares 6, 12, 24 hours ahead.

Feature Combination	Prediction Time (hour)			
	1	6	12	24
S	0.234 (0.082)	0.198 (0.069)	0.182 (0.075)	0.146 (0.089)
T	0.224 (0.124)	0.233 (0.097)	0.310 (0.084)	0.263 (0.109)
SP	0.244 (0.086)	0.192 (0.09)	0.186 (0.047)	0.200 (0.058)
S+T	0.266 (0.099)	0.214 (0.072)	0.302 (0.08)	0.253 (0.11)
S+SP	0.253 (0.096)	0.188 (0.07)	0.186 (0.086)	0.209 (0.071)
S+T+SP	0.276 (0.101)	0.216 (0.098)	0.302 (0.08)	0.289 (0.081)
S+T_PC+SP_PC	0.256 (0.074)	0.231 (0.076)	0.208 (0.078)	0.236 (0.116)
S+T+SP+A	0.276 (0.101)	0.215 (0.098)	0.303 (0.08)	0.287 (0.083)
S+T_PC+SP_PC+A	0.256 (0.074)	0.231 (0.076)	0.208 (0.078)	0.236 (0.116)

Table A.2. Average True Skill Score (TSS), based on 20 train-test split, for classifying strong (M/X) vs. weak (B/C) flares using different sets of features. Feature shorthand represents: SHARP parameter (**S**); Topology feature (**T**); Spatial Statistics feature (**SP**); Auxiliary feature (**A**); Topology feature principal component score (**T_PC**); Spatial statistics with functional principal component score for Ripley’s K function (**SP_PC**). Boldface numbers indicate that the TSS is significantly higher than the benchmark model (**S**), which is fitted only with SHARP parameters in the PIL region, across the 20 iterations. The column names labeled by 1,6,12,24 stands for the 4 datasets collected at 1,6,12,24 hours before the flare peak time.

A.3 Heidke Skill Score Results for Binary Classification

Here, as a supplemental result for Table 2, we show the Heidke Skill Score for the binary classification problem. The Heidke Skill Score (HSS) is calculated as:

$$\text{HSS} = 2 \cdot \frac{\text{TP} \times \text{TN} - \text{FN} \times \text{FP}}{(\text{FN} + \text{TP}) \times (\text{FN} + \text{TN}) + (\text{FP} + \text{TN}) \times (\text{TP} + \text{FP})}$$

where TP, TN, FN, FP are the true positive, true negative, false positive and false negative samples in the confusion matrix of the classification result.

Feature Combination	Prediction Time (hour)			
	1	6	12	24
S	0.473 (0.069)	0.478 (0.067)	0.467 (0.06)	0.413 (0.073)
T	0.501 (0.058)	0.525 (0.071)	0.504 (0.06)	0.473 (0.061)
SP	0.508 (0.058)	0.529 (0.073)	0.485 (0.068)	0.478 (0.068)
S+T	0.529 (0.072)	0.526 (0.069)	0.495 (0.056)	0.478 (0.053)
S+SP	0.514 (0.06)	0.532 (0.076)	0.481 (0.074)	0.485 (0.075)
S+T+SP	0.544 (0.071)	0.548 (0.067)	0.502 (0.069)	0.521 (0.06)
S+T_PC+SP_PC	0.525 (0.066)	0.52 (0.067)	0.486 (0.07)	0.489 (0.067)
S+T+SP+A	0.535 (0.066)	0.545 (0.059)	0.488 (0.065)	0.496 (0.059)
S+T_PC+SP_PC+A	0.542 (0.059)	0.51 (0.064)	0.488 (0.064)	0.478 (0.075)

Table A.3. Average Heidke Skill Score (HSS), based on 20 random train-test split, for classifying strong (M/X) vs. weak (B) flares using different sets of features. Standard error in brackets. Feature shorthand represents: SHARP parameter (**S**); Topology feature (**T**); Spatial Statistics feature (**SP**); Auxiliary feature (**A**); Topology feature principal component score (**T_PC**); Spatial statistics with functional principal component score for Ripley’s K function (**SP_PC**). Boldface numbers indicate that the HSS is significantly higher than the benchmark model (**S**), which is fitted only with SHARP parameters in the PIL region, across the 20 iterations. The column names labeled by 1,6,12,24 stands for the 4 datasets collected at 1,6,12,24 hours before the flare peak time.